Chemical Engineering Journal 394 (2020) 124916

Contents lists available at ScienceDirect

Chemical Engineering Journal

journal homepage: www.elsevier.com/locate/cej

CO_2 separation from flue gas mixture using [BMIM][BF_4]/MOF composites: Linking high-throughput computational screening with experiments

H. Mert Polat[a,c], Safiyye Kavak[a,c], Harun Kulak[b,c], Alper Uzun[b,c,d,*], Seda Keskin[b,c,*]

[a] Department of Materials Science and Engineering, Koc University, Rumelifeneri Yolu, 34450 Sariyer, Istanbul, Turkey
[b] Department of Chemical and Biological Engineering, Koc University, Rumelifeneri Yolu, 34450 Sariyer, Istanbul, Turkey
[c] Koc University TUPRAS Energy Center (KUTEM), Koc University, Rumelifeneri Yolu, 34450 Sariyer, Istanbul, Turkey
[d] Koc University Surface Science and Technology Center (KUYTAM), Koc University, Rumelifeneri Yolu, 34450 Sariyer, Istanbul, Turkey

HIGHLIGHTS

- High-throughput computational screening of 1085 IL/MOF composite was performed.
- Most IL/MOF composites have higher CO_2/N_2 selectivities than pristine MOFs.
- IL/MOF composites are highly promising adsorbents for flue gas separation.

ARTICLE INFO

Keywords:
Molecular simulations
Ionic liquid (IL)
Metal organic framework (MOF)
Carbon dioxide (CO_2)
Gas adsorption

ABSTRACT

In this study, we combined experiments with high-throughput molecular simulation methods to unlock CO_2/N_2 separation performances of 1085 different types of ionic liquid (IL)/metal organic framework (MOF) composites. We first validated the accuracy of our proposed computational methodology by synthesizing and characterizing three different IL/MOF composites composed of [BMIM][BF_4] (1-*n*-butyl-3-methylimidazolium tetrafluoroborate) and by comparing their experimental CO_2, N_2 adsorption and separation performances with the simulation results. Motivated from the good agreement between experiments and simulations, we performed a high-throughput computational screening of 1085 different types of MOFs and their [BMIM][BF_4]-incorporated counterparts to compute adsorption of CO_2/N_2 mixture in each material. Adsorbent performance evaluation metrics of [BMIM][BF_4]/MOF composites including selectivity, working capacity, adsorbent performance score, and regenerability were calculated and compared with those of pristine MOFs to assess adsorption-based CO_2/N_2 separation performance limits of the composite materials. Our results revealed that [BMIM][BF_4] incorporation remarkably increases CO_2 selectivity, CO_2 working capacity, and adsorption performance score of very large numbers of MOFs, resulting in excellent adsorbent candidates for separation of flue gas mixture. Analysis of the structure-performance relations showed that composites having narrow pore sizes, low porosities, and high IL loadings offer high CO_2/N_2 selectivities. These results will be useful in guiding and accelerating the design and development of new IL/MOF composites having exceptional CO_2 capture performances from flue gas mixtures.

1. Introduction

Carbon dioxide (CO_2) separation from flue gas mixture has environmental, economic, and industrial importance [1]. Emission of flue gas from the burning of fossil fuels is one of the main causes of increased CO_2 concentration in the atmosphere, which highlights the significance of CO_2 capture from flue gas [2]. In order to separate CO_2 from flue gas, many technologies, such as absorption-based separation [3], membrane-based separation [4], and cryogenic separation [5], have been used. Among these technologies, low-cost and energy efficient adsorption-based separation [6] steps forwards. For adsorption-based CO_2 separation, various adsorbent materials, such as porous carbons [7], zeolites [8], and metal organic frameworks (MOFs) [9,10] have been widely examined. MOFs, composed of metal ions connected with organic ligands, are a relatively new class of porous crystalline materials [11] and they have been considered as great candidates for CO_2 capture from flue gas [12]. MOFs have fascinating structural features, such as high surface area, high porosity, and good chemical and

* Corresponding authors at: Department of Chemical and Biological Engineering, Koc University, Rumelifeneri Yolu, 34450 Sariyer, Istanbul, Turkey.
E-mail addresses: auzun@ku.edu.tr (A. Uzun), skeskin@ku.edu.tr (S. Keskin).

https://doi.org/10.1016/j.cej.2020.124916
Received 20 January 2020; Received in revised form 9 March 2020; Accepted 27 March 2020
Available online 03 April 2020
1385-8947/ © 2020 The Author(s). Published by Elsevier B.V. This is an open access article under the CC BY-NC-ND license (http://creativecommons.org/licenses/BY-NC-ND/4.0/).

thermal stability [13], which make them promising materials for many applications, such as catalysis [14], electrochemical energy storage [15], chemical sensing [16], gas adsorption and separation [9,17]. One of the most remarkable advantages of MOFs is that their physical and chemical properties can be tuned by the post-synthesis modification methods [18–20] to achieve high performance gas adsorption and separation [21,22].

Post-synthesis modification of MOFs using ionic liquids (ILs) to tailor the gas uptake and selectivity of materials has a great potential [23]. ILs are molten salts that are composed of organic cations and organic or inorganic anions and they show high thermal and chemical stabilities, negligible vapor pressures, and high gas affinities [24]. Because of these exceptional properties, ILs have been utilized in many fields, such as synthesis [25], catalysis [26], gas absorption and separation [27,28]. Similar to MOFs, an almost infinite number of ILs with tunable properties can be synthesized using different combinations of anions and cations. In recent years, two approaches have been introduced to synthesize IL/MOF composites, either coating the external surface of MOFs using ILs [29] or incorporation of ILs into the pores of MOFs [30–32]. Both approaches are shown to provide significant enhancements in gas adsorption and separation performance of MOFs since they combine the desired properties of two different families of materials: high porosity and large surface area of MOFs with high gas affinity of ILs [23]. Existence of very large numbers of possible IL-MOF pairs offers a broad opportunity to generate IL/MOF composites with various properties, but on the other hand, it is not straightforward to experimentally synthesize and test every single composite material for a target gas separation. Computational methods, especially molecular simulations, play an important role in this field to screen large numbers of materials with the aim of identifying the best candidates for a target application.

Molecular simulations have been widely used to screen MOFs for various gas adsorption and separation processes, such as CH_4, O_2, H_2 storage, noble gas separation, separation of organic molecules, such as xylene and benzene, and CO_2 separation [33–35]. ILs have been also examined using molecular simulations to select the best ones for the absorption and separation applications, such as separation of ethylene from acetylene [36], benzene separation from hydrocarbons [37], dibenzothiophene (DBT) and dibenzothiophene 5,5-dioxide ($DBTO_2$) separation from hydrocarbons [38,39] and CO_2 [40], and SO_2 [40] absorption. Molecular simulations have been recently used to examine the potential of IL/MOF composites in CO_2/N_2 [41–46], CO_2/CH_4 [42–44,47], CH_4/N_2 [44], and H_2S/CH_4 [48] separations as we will briefly discuss here. Chen et al. [41] showed that 1-*n*-butyl-3-methylimidazolium hexafluorophosphate ([BMIM][PF_6])/IRMOF-1 composite is more selective towards CO_2 over N_2 than pristine IRMOF-1 using grand canonical Monte Carlo (GCMC) simulations. Vicent-Luna et al. [42] performed GCMC simulations on five different IL/CuBTC composites and showed that CO_2/CH_4 and CO_2/N_2 selectivities of CuBTC enhance significantly at low pressures upon IL incorporation. They also showed that incorporation of ILs into covalent organic frameworks (COFs) leads to increase in their CO_2/CH_4 selectivities [49]. Four different 1-*n*-ethyl-3-methylimidazolium thiocyanate ([EMIM][SCN])/MOF composites were studied using the density functional theory (DFT) calculations, molecular dynamics (MD) and GCMC simulations and results showed that increasing IL loading leads to higher CO_2 selectivity over CH_4 and N_2 [44]. Li et al. [48] showed that IL-incorporation into Cu-TDPAT increases H_2S/CH_4 selectivity of the material. Xue et al. [43] performed GCMC simulations on both IL/MOF and IL/COF composites and showed that better dispersion of IL molecules inside the pores leads to higher CO_2/CH_4 and CO_2/N_2 selectivity. Gupta et al. performed GCMC [45] and MD [46] simulations to study CO_2 separation performance of 1-*n*-butyl-3-methylimidazolium thiocyanate [BMIM][SCN]-incorporated IRMOF and ZMOF. Lan et al. [47] recently studied composites of hypothetical, computer-generated MOFs and two different ILs, 1,3-dimethylimidazolium tetrafluoroborate ([MMIM][BF_4]) and 1-*n*-butyl-3-methylimidazolium bis(trifluoromethanesulfonyl)imide ([BMIM][NTf_2]), for CO_2/CH_4 adsorption. Studying very large numbers of hypothetical MOFs is very useful but synthesizability of most hypothetical MOFs remains unclear [50] and therefore, it is not possible to compare the simulated separation performance of IL-incorporated hypothetical MOFs with the experimentally measured performance. Our group reported a good agreement between GCMC simulations and experimental single-component adsorption isotherms of CO_2, CH_4, and N_2 for [BMIM][PF_6]/ZIF-8 composite [30]. Ideal CO_2/CH_4 and CO_2/N_2 selectivities of the composite were found to be at least two-times higher than those of pristine ZIF-8. 1-*n*-butyl-3-methylimidazolium tetrafluoroborate ([BMIM][BF_4])/ZIF-8 composite was also examined combining experiments with molecular simulations and a good agreement was shown between experiments and simulations for CO_2, CH_4, N_2 adsorption and their heat of adsorption values [51].

Recently, we proposed a molecular simulation methodology to screen IL/MOF composites by investigating seven different IL/CuBTC composites where ILs were composed of the same cation, 1-*n*-butyl-3-methylimidazolate ($[BMIM]^+$) with different anions [52]. The force field that best represents the experimental CO_2, CH_4, and N_2 adsorption isotherms of IL/CuBTC composites was identified and our computational methodology was validated by comparing the results with experimentally measured gas uptakes of two newly synthesized composites, 1-*n*-butyl-3-methylimidazolium dicyanamide ([BMIM][DCA])/CuBTC and 1-*n*-butyl-3-methylimidazolium dibutylphosphate ([BMIM][DBP])/CuBTC. Although these studies have been very promising to reveal the single-component gas adsorption properties of IL/MOF composites, we currently have a very limited knowledge on the gas separation, especially on the flue gas mixture separation potential of IL/MOF composites. Since only a few different MOF structures, mostly CuBTC and ZIF-8, have been examined for IL/MOF composites to date, identifying the adsorbent performance limits of large variety of IL/MOF composites has not been possible.

In this work, we aimed to unlock CO_2/N_2 separation performance limits of IL/MOF composites combining experiments with a high-throughput computational screening method. For this aim, we considered one of the most widely studied, commercially available, low-cost ILs, [BMIM][BF_4]. We first validated the accuracy of our proposed computational methodology by synthesizing and characterizing three different [BMIM][BF_4]/MOF composites and by comparing their experimental CO_2, N_2 adsorption and separation performances with the simulation results. Motivated from the good agreement between experiments and simulations, we performed a high-throughput computational screening of 1085 different types of real MOFs and their [BMIM][BF_4]-incorporated counterparts to compute adsorption of CO_2/N_2 mixture in each material. Using the results of molecular simulations, various adsorbent performance evaluation metrics including selectivity, working capacity, adsorbent performance score, and regenerability were calculated for pristine MOFs and [BMIM][BF_4]/MOF composites to assess the impact of the presence of ILs in the pores of MOFs on the adsorption-based CO_2/N_2 separation performances of materials. Finally, structure-performance relations of [BMIM][BF_4]/MOF composites were investigated to understand which structural characteristics of materials lead to the composites with high CO_2/N_2 selectivities. These results will be useful to guide the design and development of new IL/MOF composites having high CO_2 separation performance.

2. Methods

2.1. Computational methods

In this work, we specifically focused on [BMIM][BF_4] since it is a widely studied IL in addition to being one of the smallest ILs reducing the computational cost during the IL incorporation into MOFs. We initially started with a MOF library consisting of 3816 different structures [53]. The crystal files of all MOFs were taken from the non-disordered

MOF subset of the Cambridge Structural Database (CSD) and solvents were removed from the structures using the Python code of the CSD subset [54] to mimic the experimental activation procedure. We discarded MOFs that have pore limiting diameters (PLDs) < 6 Å, the approximate length between the furthest fluorine atom in the anion and the furthest hydrogen atom in the cation of [BMIM][BF_4], to ensure successful incorporation of IL molecules into the pores of MOFs. After this restriction, we ended up with 1085 different MOF structures.

GCMC simulations were used as implemented in the RASPA [55] to compute adsorption of CO_2/N_2 mixture in pristine MOFs and IL-incorporated MOFs. We used the Dreiding force field [56] for both [BMIM][BF_4] and MOF atoms. For metal atoms whose intermolecular interaction parameters are not present in Dreiding force field, Universal Force Field (UFF) was used [57]. Force field parameters used to describe the MOFs and [BMIM][BF_4] are listed in Table S1 of Supporting Materials (SM). We modeled CO_2 molecule as a three-site rigid molecule with 12–6 Lennard-Jones (LJ) potential where the point charges were located at the center of each site [58]. N_2 molecule was also modeled as three-site molecule. Center of N atoms in N_2 molecule had both LJ potential and point charge while the site at the center of mass only had a point charge to describe the quadrupole moment of the molecule [59]. Table S2 shows the details of gas models. Lorentz-Berthelot mixing rules were used to calculate the cross-atomic force field parameters. In all simulations, cut-off distance for interatomic interactions was set to 12 Å. We considered all MOFs and IL molecules as rigid structures to reduce the computational expense and facilitate the high-throughput material screening. Since we only focused on MOFs that have PLDs > 6 Å, adsorbate molecules are relatively small compared to the pore size of MOFs and flexibility is expected to have a negligible effect on the simulated gas uptakes as previously shown in the literature [60]. The isosteric heat of adsorption values (Q_{st}) for CO_2/N_2 mixture were also calculated using fluctuations in potential energy of the system. Structural characteristics of pristine MOFs and [BMIM][BF_4]/MOF composites such as porosities, PLDs and the largest-cavity diameters (LCD) were calculated using Zeo++ software [61]. We used the Baker's minimization method with NVT ensemble to incorporate the IL molecules into MOFs as described in our previous work [52]. IL loading was set to 1 IL molecule per unit cell of a MOF. Translation, rotation, and random translation moves were used to incorporate ILs into MOFs. Then, the energy minimization algorithm was run until the root-mean-square gradient and maximum gradient were lower than 10^{-6}. In the minimization procedure, point charges were assigned to MOFs using charge equilibration (QEq) method [62] as implemented in the RASPA. Atomic coordinates and point charges of [BMIM][BF_4] were taken from our previous work [52], where they were calculated using the DFT calculations. After IL incorporation, point charges were reassigned to [BMIM][BF_4]/MOF composites, again using the QEq method, to calculate the electrostatic interactions between the adsorbates and atoms of IL/MOF composites.

In GCMC simulations, 5×10^4 and 5×10^5 cycles were performed for initialization and for taking the ensemble averages, respectively. We used five different moves, namely, translation, reinsertion, rotation, swap, and identity exchange. GCMC simulations were performed at an adsorption (desorption) pressure of 1 (0.1) bar at 25 °C to mimic the conditions of vacuum swing adsorption processes for CO_2/N_2:15/85 mixture that represents the flue gas stream [63]. Pressures were converted to fugacity using the Peng-Robinson equation of state. Results of CO_2/N_2:15/85 mixture adsorption simulations were used to compute adsorbent performance evaluation metrics; selectivity (S), working capacity (ΔN), regenerability (R%) and adsorbent performance score (APS) as described in Table 1. Single-component CO_2 adsorption simulations were also performed for three selected IL/MOF composites ([BMIM][BF_4]-incorporated UiO-66, ZIF-8, and CuBTC) using the same parameters as described above except the identity exchange move. We used the CSD entries with refcodes FIQCEN, RUBTAK, and FAWCEN01 for CuBTC, UiO-66, and ZIF-8, respectively. We note that RUBTAK was missing hydrogen atoms in its CSD-deposited crystal file and we added the required hydrogen atoms into the structure using the Forcite module of Material Studio software 2017 R2 [64]. In this geometry optimization calculation, "Smart" algorithm was used with convergence criteria of 2×10^{-5} kcal/mol, 10^{-3} kcal/mol/Å, 10^{-3} GPa and 10^{-5} Å for energy, force, stress and displacement, respectively. Atomic representations of CuBTC, UiO-66, ZIF-8 and [BMIM][BF_4] are shown in Fig. S1. The void fractions of these three [BMIM][BF_4]/MOF composites were calculated using Zeo++ software with a probe diameter of 0 Å and they were used to convert the absolute gas uptakes to excess uptakes to compare the results of simulations with the experimental measurements.

Table 1
Adsorbent performance evaluation metrics used in this study to evaluate the separation performance of pristine MOFs and IL/MOF composites.

Parameter	
Selectivity	$S_{CO_2/N_2} = \frac{x_{CO_2}/x_{N_2}}{y_{CO_2}/y_{N_2}}$
CO_2 working capacity	$\Delta N_{CO_2} = N_{ads,CO_2} - N_{des,CO_2}$
Regenerability	$R\% = \frac{\Delta N_{CO_2}}{N_{ads,CO_2}} \times 100$
Adsorbent Performance Score	$APS = S_{ads,CO_2/N_2} \times \Delta N_{CO_2}$

* N_{ads,CO_2} (N_{des,CO_2}) is the simulated CO_2 uptake at adsorption (desorption) pressure. x and y represent the adsorbed and bulk gas composition, respectively. We note that ideal selectivities of materials were calculated only by dividing the single-component CO_2 uptake with N_2 uptake, without normalizing by the bulk gas composition.

2.2. Experimental methods

2.2.1. Materials

In this work, one new [BMIM][BF_4]/MOF composite, namely [BMIM][BF_4]/UiO-66 (3.34 wt% IL loading), and two previously reported [BMIM][BF_4]/MOF composites but with different IL loadings than their original reports, [BMIM][BF_4]/ZIF-8 (7.8 wt% IL loading) [51] and [BMIM][BF_4]/CuBTC (2.38 wt% IL loading) [21], were synthesized. For this purpose, [BMIM][BF_4] (> 97%), CuBTC (Basolite C300), and ZIF-8 (Basolite Z1200) were purchased from Sigma Aldrich. UiO-66 and acetone (> 99.8%) were purchased from ACSYNAM, Canada and Merck, respectively. We stored [BMIM][BF_4] and MOFs in an Ar (> 99.999%, Linde) glovebox (Labconco) prior to usage. [BMIM][BF_4] was dried at 80 °C for 6 h and kept under vacuum for 12 h before being transferred to the glovebox [65]. All MOFs were activated at 125 °C under vacuum overnight before usage.

2.2.2. Composite synthesis

Composites were synthesized for a target IL loading of only one IL molecule per MOF cage. For this purpose, first, 22.8, 78.3, and 33.4 mg of [BMIM][BF_4] were dissolved in 20 mL acetone for 1 h to prepare 1 g of [BMIM][BF_4]/CuBTC, [BMIM][BF_4]/UiO-66, and [BMIM][BF_4]/ZIF-8 samples with loadings of 2.3, 3.3, and 7.8 wt%, respectively. Then the required amount of MOFs (977.2 mg for [BMIM][BF_4]/CuBTC, 966.6 mg for [BMIM][BF_4]/UiO-66, and 921.7 mg for [BMIM][BF_4]/ZIF-8) were added into the solution and the solution was mixed at 35 °C under open atmosphere until the solvent was completely evaporated. We then dried the samples completely at 105 °C overnight and stored them in a desiccator until the usage to protect them from humidity and other impurities.

2.2.3. Characterization methods

2.2.3.1. X-ray diffraction (XRD). A Bruker D8 Advance X-ray diffractometer was used to obtain the XRD patterns of CuBTC, ZIF-8, UiO-66, and their [BMIM][BF_4]-incorporated composites. The diffractometer was equipped with a Lynxeye detector and a slit of

1 mm. X-ray generator was operated at 30 kV voltage and 10 mA current to produce Cu Kα1 radiation. The analyses were performed in the 2θ range of 5-50° with a resolution of 0.0204°.

2.2.3.2. Scanning electron microscopy (SEM). We used a Zeiss Ultra Plus Field-Emission SEM (FESEM) to obtain the SEM images of pristine MOFs and [BMIM][BF_4]/MOF composites. An accelerating voltage of 3 kV and a working distance of 4 mm were used in the analyses. Prior to imaging, materials were coated with gold to prevent charging during imaging and attached to a pin mount sample holder using carbon tape.

2.2.3.3. Fourier transform infrared (FTIR) spectroscopy. A Thermo Scientific Nicolet iS50 FTIR spectrometer equipped with an attenuated total reflection (ATR) cell was used to obtain the FTIR spectra of pristine MOFs and [BMIM][BF_4]/MOF composites. 128 (512) samples were collected for background (sample) between 650 and 4000 cm^{-1} with a resolution of 2 cm^{-1}.

2.2.3.4. Brunauer-Emmett-Teller (BET) surface area. We used a Micromeritics ASAP 2020 physisorption analyzer to perform BET analyses of pristine MOFs and [BMIM][BF_4]/MOF composites. Approximately 200 mg of sample was used in these analyses and all samples were activated at 125 °C prior to the analyses. Then, the samples were cooled down to −196 °C using liquid nitrogen and free space measurements were done using helium gas. We obtained N_2 gas adsorption isotherms of the samples at −196 °C and between 10^{-6}-1 bar. BET surface area of the materials was calculated by fitting the isotherm to the BET equation by using the relative pressure range of 0.06–0.3.

2.2.3.5. X-ray fluorescence (XRF) spectroscopy. A Bruker S8 Tiger XRF spectrometer was used for elemental analysis of [BMIM][BF_4]/CuBTC, [BMIM][BF_4]/UiO-66, and [BMIM][BF_4]/ZIF-8. The analysis was performed under vacuum. A rhodium anode was used in the X-ray generator and the generator was set to 4 kW power. SpectraPlus Eval2 v.2.2.454 software was used for data analysis.

2.2.3.6. Thermogravimetric analysis (TGA). Thermal stabilities of pristine MOFs, [BMIM][BF_4]/MOF composites, and bulk [BMIM][BF_4] were determined by using a TA Instruments Q500 thermogravimetric analyzer. In the analyses, a platinum pan and approximately 15 mg of sample was used. Temperature ramp of 5 °C/min was used until the temperature reached 100 °C. Then, an isothermal treatment for 8 h at 100 °C was performed to ensure that moisture in the samples was completely eliminated. Finally, a temperature ramp of 2 °C/min was applied until the temperature reached 700 °C. N_2 flow rate of 40 (60) mL/min was used as balance (purge) gas. Onset (T_{onset}) and derivative onset (T'_{onset}) temperatures of the samples were obtained from thermogravimetry and derivative termogravimetry curves, respectively. We used T'_{onset} temperature as decomposition temperature in this study, because T_{onset} generally overestimates the thermal decomposition temperature [30].

2.2.4. Gas adsorption measurements

We used a Micromeritics HPVA-II-200 high pressure volumetric analyzer to obtain CO_2 (> 99.9 vol%, Linde) and N_2 (> 99.998 vol%, Linde) adsorption isotherms of pristine MOFs and [BMIM][BF_4]/MOF composites. Before the measurements, we activated approximately 350 mg of sample at 125 °C until the pressure inside the sample holder reached to 10^{-6} bar. We then purged the system three-times with helium gas to eliminate impurities from previous measurements. All gas adsorption measurements were performed in a pressure range of 0.1–10 bar at 25 °C.

Table 2
Elemental analysis and calculated IL loadings of [BMIM][BF_4]/CuBTC, [BMIM][BF_4]/UiO-66, and [BMIM][BF_4]/ZIF-8.

Composite	Concentration (wt.%)	Calculated IL loading (wt.%)
[BMIM][BF_4]/CuBTC	Cu: 27.05 B: 0.27	2.15
[BMIM][BF_4]/UiO-66	Zr: 24.16 B: 0.12	3.44
[BMIM][BF_4]/ZIF-8	Zn: 34.93 B: 0.47	7.48

3. Results and discussions

3.1. Comparison of experiments and simulations

We first tested the accuracy of our computational approach by experimentally synthesizing, characterizing, and calculating CO_2/N_2 selectivities and CO_2 working capacities of three different [BMIM][BF_4]/MOF composites, composed of CuBTC, UiO-66, and ZIF-8. We specifically chose UiO-66, ZIF-8, and CuBTC to validate our computational approach because these MOFs are (a) the most widely studied MOFs in the literature hence detailed structural information is available, (b) commercially available to experimentally synthesize IL/MOF composites, (c) they are purchased directly from vendors with proven reliability, the composites could be successfully reproduced in every batch, which would not be possible if the MOFs were synthesized in house as the synthesis might result in low yields for some MOFs leading to reproducibility problems. Before focusing on the comparison of experimental and simulated gas adsorption and separation performances of these composites, we first discuss characterization results. XRF spectroscopy was studied to confirm the successful IL incorporation and Table 2 shows the elemental analysis of [BMIM][BF_4]/CuBTC, [BMIM][BF_4]/UiO-66, and [BMIM][BF_4]/ZIF-8 composites and their calculated IL loadings. XRF spectroscopy results showed that all three composites comprise boron, demonstrating successful incorporation of [BMIM][BF_4] into MOFs. Comparison of the actual IL loadings calculated from the XRF spectroscopy and targeted IL loadings (2.3, 7.8, and 3.3 wt% for [BMIM][BF_4]/CuBTC, [BMIM][BF_4]/UiO-66, and [BMIM][BF_4]/ZIF-8, respectively) indicates that targeted IL loadings were successfully achieved. The BET surface areas of these materials calculated from N_2 adsorption isotherms at −196 °C (Fig. S2) further confirms the successful [BMIM][BF_4] incorporation as the surface areas of pristine MOFs, 1325, 750, and 1208 m^2/g for CuBTC, UiO-66, and ZIF-8, decreased to 909, 578, and 972 m^2/g for [BMIM][BF_4]/CuBTC, [BMIM][BF_4]/UiO-66, and [BMIM][BF_4]/ZIF-8, respectively, upon IL incorporation.

Fig. 1 shows XRD patterns, TG curves, FTIR spectra, CO_2 and N_2 uptakes of pristine MOFs, CuBTC, UiO-66, and ZIF-8, and their corresponding [BMIM][BF_4]-incorporated composites. Fig. 1(a) shows that there is no change in the XRD peaks of pristine MOFs upon IL incorporation except for some changes in the intensity. These results showed that crystal structures of pristine MOFs were preserved upon IL incorporation. It should be noted that the changes in the intensity of some of the features may be associated with slight alterations in the electronic structure of the pristine MOFs upon IL incorporation. Furthermore, SEM images shown in Figs. S3-S5 illustrate that crystal size and shape did not significantly change upon [BMIM][BF_4] incorporation. Fig. 1(b) shows the TG curves of the bulk [BMIM][BF_4], pristine MOFs, and [BMIM][BF_4]/MOF composites. DTG curves of these materials are also given in Fig. S6. According to these results, T'_{onset} temperatures of CuBTC, UiO-66, and ZIF-8 were found as 324, 480, and 365 °C, respectively. However, T'_{onset} temperatures of three composites were lower than those of their corresponding pristine MOFs and bulk [BMIM][BF_4] (350 °C) as they were 304, 293, and 310 °C for [BMIM][BF_4]/CuBTC, [BMIM][BF_4]/UiO-66, and [BMIM][BF_4]/ZIF-8,

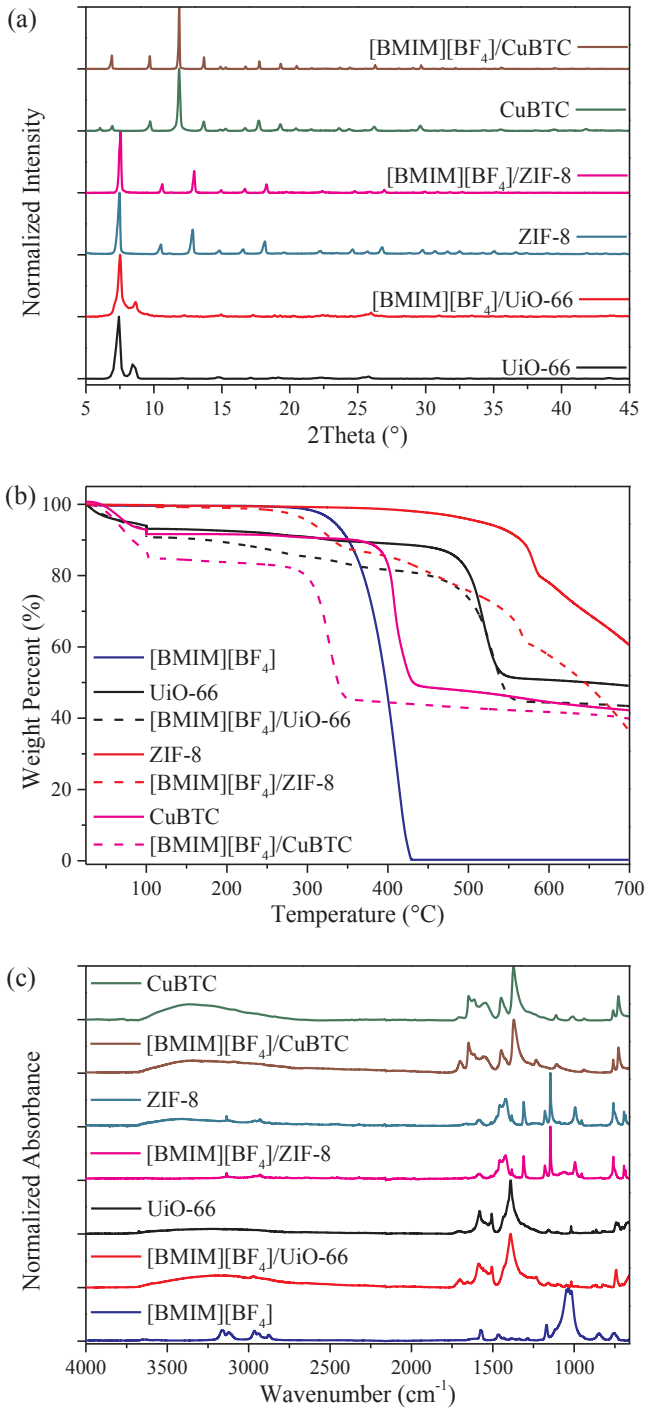


Fig. 1. (a) XRD patterns, (b) TGA curves, (c) FTIR spectra of [BMIM][BF_4]/MOF composites and pristine MOFs.

respectively. These decreases in the T'_{onset} temperatures were possibly because of the slight changes in the structure of the constituents of these composites [52]. Results indicated that there were direct interactions between [BMIM][BF_4] and MOFs in the composites, and these interactions alter the thermal decomposition mechanisms.

Fig. 1(c) shows the FTIR spectra of bulk IL, pristine MOFs, and [BMIM][BF_4]/MOF composites. Vibrational modes were assigned to the peaks in the FTIR spectrum of [BMIM][BF_4] according to the literature [66,67]. Symmetric (ν_s(B-F)) and asymmetric stretching mode of B-F bond (ν_{as}(B-F)) of the anion were assigned to peaks centered at 751 and 1021 cm^{-1}, respectively, in the FTIR spectrum of [BMIM][BF_4]. ν_s(B-F)

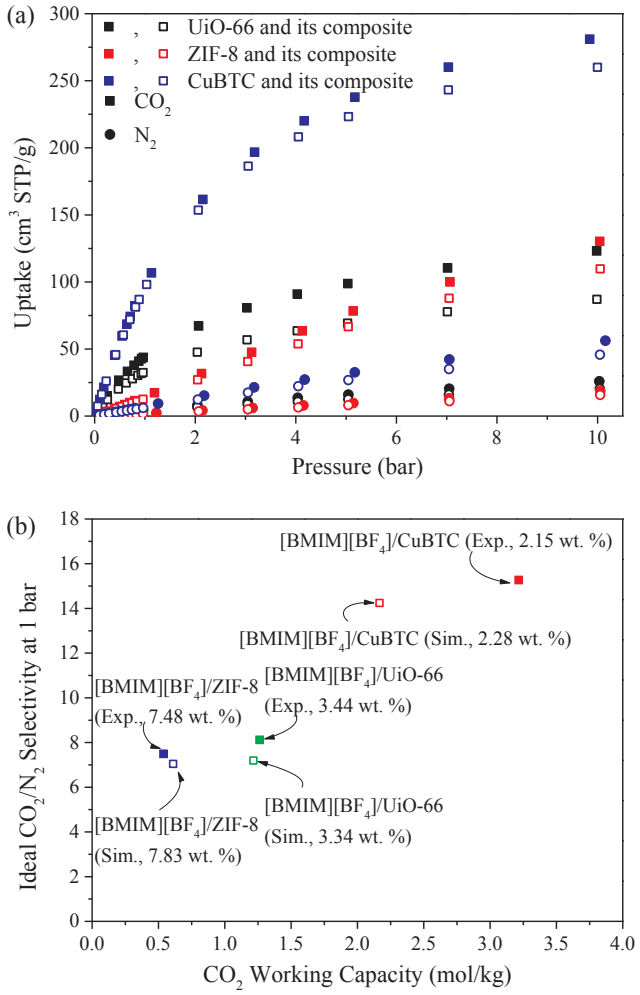


Fig. 2. (a) CO_2 and N_2 gas adsorption isotherms of [BMIM][BF_4]/MOF composites and pristine MOFs. (b) Comparison of experimental and simulated CO_2/N_2 selectivity and CO_2 working capacity of [BMIM][BF_4]/CuBTC, [BMIM][BF_4]/ZIF-8 and [BMIM][BF_4]/UiO-66 composites.

shifted to 802, 806, and 768 cm^{-1} in [BMIM][BF_4]/CuBTC, [BMIM][BF_4]/UiO-66, and [BMIM][BF_4]/ZIF-8, respectively, upon the incorporation of IL into the corresponding MOF. ν_{as}(B-F) shifted from 1021 cm^{-1} to 1071, 1034, and 1036 cm^{-1} upon the incorporation of [BMIM][BF_4] into CuBTC, UiO-66, and ZIF-8, respectively. Additionally, ν_s(–C2H) mode exhibited blue shifts from 3126 cm^{-1} to 3137, 3137, and 3145 cm^{-1} upon IL-incorporation to CuBTC, UiO-66, and ZIF-8, respectively. These shifts in the characteristic vibrational modes of [BMIM][BF_4] were because of the slight changes in the structure of IL as we mentioned, indicating the presence of direct interactions between [BMIM][BF_4] and pristine MOFs in the composite structures, consistent with the TGA results.

Fig. 2(a) shows experimentally measured single-component CO_2 and N_2 adsorption isotherms of pristine MOFs and [BMIM][BF_4]/MOF composites in a pressure range of 0.1–10 bar at 25 °C. For all composites, CO_2 and N_2 uptakes at all pressures were measured to be lower than those of their corresponding pristine MOFs. Fig. S7 demonstrates ideal CO_2/N_2 selectivities of [BMIM][BF_4]/MOF composites and MOFs calculated using the models fitted to the single-component gas uptakes as a function of pressure. Parameters used to fit the dual-site Langmuir (N_2) and Freundlich (CO_2) models are given in Tables S3-S6. Data showed that [BMIM][BF_4]/CuBTC and [BMIM][BF_4]/ZIF-8 offer improved CO_2 separation performance especially at lower pressures. [BMIM][BF_4]/UiO-66 has slightly lower selectivity than pristine UiO-

66 at all pressures. This insignificant decrease in CO_2/N_2 selectivity may be expected because this composite has a very low IL loading (3.44 wt%) and as shown in literature [21,51], higher IL loadings generally lead to increases in ideal CO_2/N_2 selectivity of MOFs.

We then compared experimental CO_2/N_2 selectivity and CO_2 working capacity of synthesized [BMIM][BF_4]/MOF composites with the simulated values in Fig. 2(b). Ideal CO_2/N_2 selectivity of [BMIM][BF_4]/CuBTC, [BMIM][BF_4]/UiO-66, and [BMIM][BF_4]/ZIF-8 composites were calculated as 15.3, 8.1, and 7.5 at 1 bar, respectively, based on the experimentally measured single-component gas uptakes. Molecular simulations predicted these selectivities as 14.3, 7.2, and 7.0, respectively. This comparison showed that our computational screening approach accurately predicts CO_2/N_2 selectivities of [BMIM][BF_4]/MOF composites. Simulated CO_2 working capacity of these materials, which were calculated using CO_2 uptakes at adsorption (desorption) pressure of 1 (0.1) bar, were also predicted to be in a good agreement with experimentally measured values except for the underestimation of CO_2 working capacity for [BMIM][BF_4]/CuBTC. Here, we note that molecular simulations of MOFs having open metal sites, such as CuBTC, may need a pressure dependent scaling factor to better fit the simulated and experimental gas adsorption data, as we recently reported [52].

3.2. Screening of [BMIM][BF_4]/MOF composites for mixture separation

Motivated from the good agreement between experiments and molecular simulations for ideal selectivity and working capacity as shown above, we applied the same computational approach to assess CO_2/N_2 mixture adsorption and separation performances of 1085 different [BMIM][BF_4]/MOF composites. CO_2/N_2 selectivity, CO_2 working capacity, APS, and R% of all [BMIM][BF_4]-incorporated MOFs were computed and compared with those of pristine MOFs to discover the potential of IL/MOF composites for flue gas separation using GCMC simulations. Fig. 3(a) illustrates the predicted CO_2/N_2 selectivities of MOFs and [BMIM][BF_4]-incorporated MOFs as a function of their CO_2 working capacities at an adsorption (desorption) pressure of 1.0 (0.1) bar at 25 °C. CO_2/N_2 selectivities of pristine MOFs were calculated to be between 1.8 and 1184.1 and their CO_2 working capacities were found to be in the range of 0.01–2.9 mol/kg. Mixture selectivities of [BMIM][BF_4]/MOF composites were computed to range from 2.1 to 2706.2 whereas their CO_2 working capacities were calculated to be 0.01–2.3 mol/kg, indicating that selectivities of most MOFs were enhanced upon the IL incorporation without sacrificing from the working capacities.

In order to quantify the performance enhancements obtained by IL incorporation into MOFs, normalized CO_2 selectivity and normalized CO_2 working capacity of composites are shown in Fig. 3(b). Normalized values were calculated by dividing the computed metric of IL/MOF composite by that of corresponding pristine MOF. Normalized selectivities of IL/MOF composites varied between 0.8 and 25.4 while their normalized CO_2 working capacities were between 0.1 and 5.9. Although some MOFs showed a slight decrease in CO_2 selectivity upon IL incorporation, majority of MOFs that we studied (97.6% of MOFs) showed higher CO_2/N_2 selectivity upon IL incorporation than their pristine counterparts did. Similarly, CO_2 working capacities of 82.8% of MOFs (898 of 1085 MOFs) increased upon IL incorporation. One remarkable outcome from our simulations is that 82.4% of MOFs (894 of 1085) showed both increased CO_2 selectivity and enhanced CO_2 working capacity upon [BMIM][BF_4] incorporation. Data show that there are [BMIM][BF_4]/MOF composites that offer exceptionally higher performance than their pristine counterparts, such as up to 25-times higher CO_2/N_2 selectivity along with up to six-times higher CO_2 working capacity than their pristine MOFs. These results highlight the exceptional potential of IL/MOF composites for CO_2 separation from flue gas mixture. It is important to note that these improvements in performance metrics were achieved by the incorporation of only one IL molecule per unit cell of the MOF.

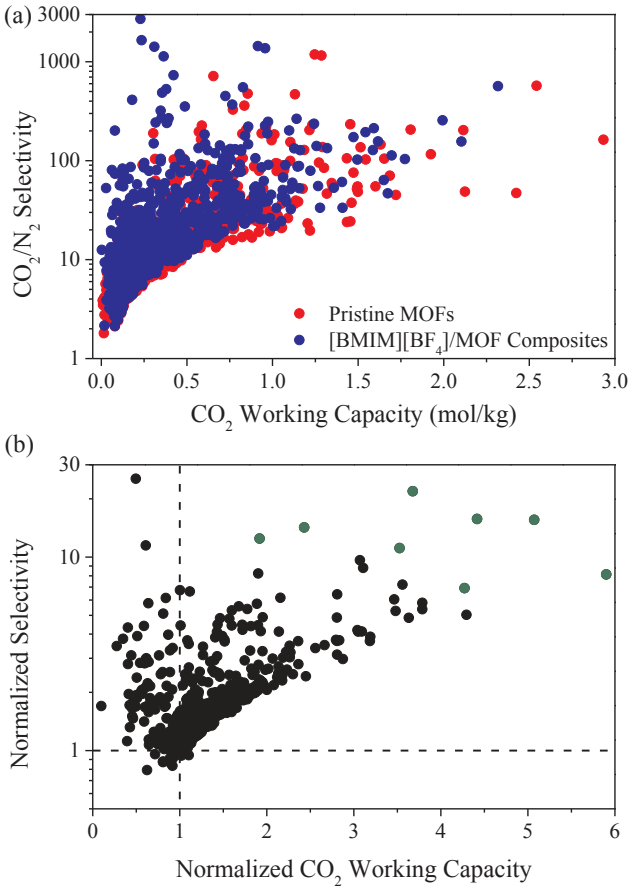


Fig. 3. (a) CO_2 selectivities and CO_2 working capacities of [BMIM][BF_4]/MOF composites and pristine MOFs. (b) Normalized CO_2 selectivity and normalized CO_2 working capacity of [BMIM][BF_4]/MOF composites. Black dashed lines in (b) represent the border for increase or decrease of metrics. Green data points in (b) show [BMIM][BF_4]/MOF composites that have at least 10-times higher CO_2 selectivity or 4-times higher CO_2 working capacity than their pristine MOFs without satisfying the minimum desired R% of 85%. (For interpretation of the references to colour in this figure legend, the reader is referred to the web version of this article.)

Both selectivity and working capacity are widely used in the evaluation and selection of the adsorbent materials. In addition to high selectivity and working capacity, it is also desired to have a high R% for an economic gas separation process. Our group recently showed that using APS, the multiplication of selectivity and working capacity, together with R% is a very useful strategy to efficiently identify the most promising adsorbents, since there is generally a trade-off between APS and R% [53]. When we specifically focused on highly promising IL/MOF composites, such as the ones exhibiting normalized CO_2/N_2 selectivities > 10 or normalized CO_2 working capacities > 4, we found that almost all of them were calculated to have an R% $< 85\%$ as shown by green data points in Fig. 3(b). The refcodes of these promising MOFs are available in Table S7 of SM. In other words, IL/MOF composites exhibiting significantly higher CO_2/N_2 selectivity and higher CO_2 working capacity than those of their corresponding pristine MOFs generally suffer from low R%. In order to identify the composites that offer the best combination of CO_2 selectivity, CO_2 working capacity, and R%, we plotted the calculated R% of materials as a function of their APSs in Fig. 4(a). Results showed that 87.6% of the pristine MOFs have an R% higher than the minimum desired value of 85%, while 72.8% of [BMIM][BF_4]/MOF composites exceeded this value. There is a trade-off between R% and APS; MOFs having a high APS suffer from a low R% and vice versa. IL incorporation does not make a significant change in the APSs of MOFs which already have high values but it has a positive

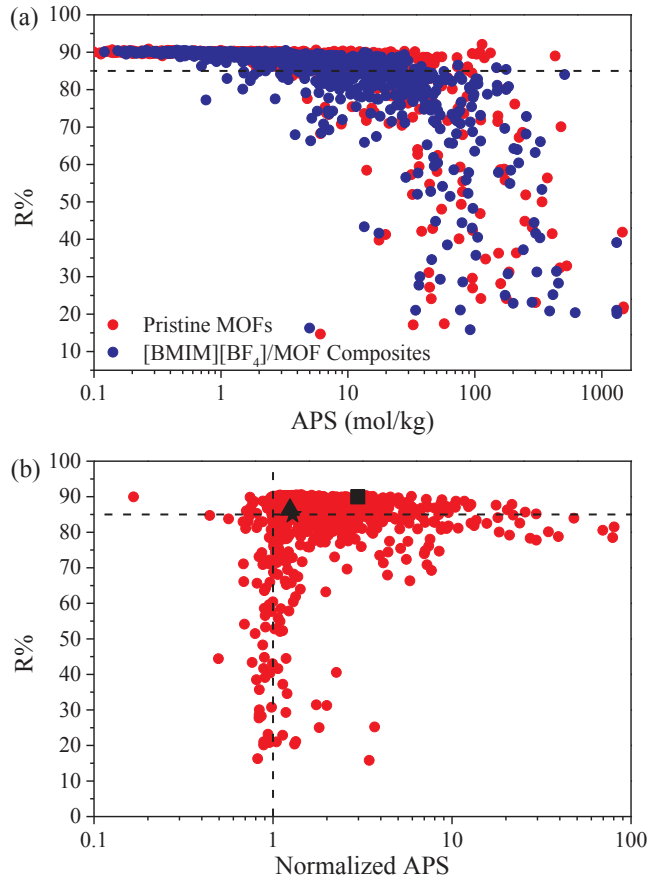


Fig. 4. (a) R% and APS of pristine MOFs and [BMIM][BF_4]/MOF composites. (b) R% and normalized APS of [BMIM][BF_4]/MOF composites. The dashed lines show the minimum desired value of R% (85%). Vertical black dashed line in (b) represents the border for increase/decrease in APSs of materials upon IL incorporation. Black symbols in (b) represent [BMIM][BF_4]-incorporated CuBTC (triangle), [BMIM][BF_4]-incorporated UiO-66 (star) and [BMIM][BF_4]-incorporated ZIF-8 (square).

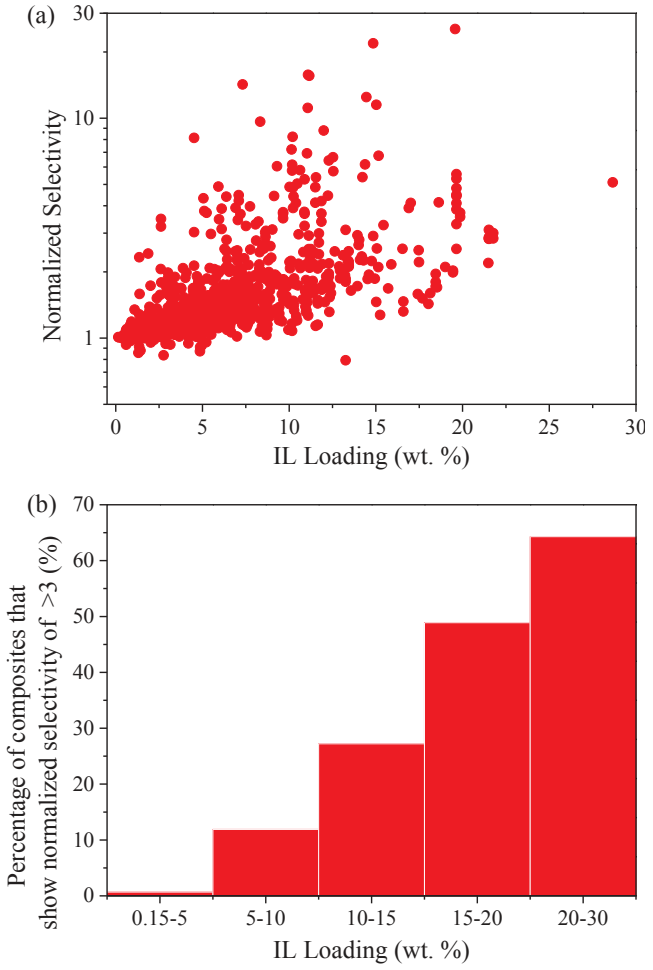


Fig. 5. (a) Normalized selectivity of [BMIM][BF_4]/MOF composites as a function of IL loading (wt.%). (b) Percentage of IL/MOF composites which are three-times more selective than their corresponding pristine MOFs for different ranges of IL loading.

impact on the MOFs having relatively low APSs. For example, a very small number of pristine MOFs, 38 among 1085, was calculated to have APSs > 100 mol/kg and this number increased up to 46 upon [BMIM][BF_4] incorporation. Fig. 4(b) demonstrates R% and normalized APSs of [BMIM][BF_4]/MOF composites. Accordingly, 92.3% of [BMIM][BF_4]/MOF composites showed higher APS than their corresponding pristine MOFs and APS values of 31 MOFs increased more than 10-times upon IL-incorporation while 13 of them retained the minimum desired value of R% (85%).

Although each IL/MOF composite considered here has an IL loading of only one IL molecule per unit cell of MOF, the corresponding IL loading in wt% varies. Fig. 5(a) shows the normalized selectivities of IL/MOF composites as a function of the IL loading which was calculated in terms of wt% using the unit cell volume of MOFs, theoretical crystal density of MOFs, and molar weight of [BMIM][BF_4] as demonstrated in the SM. IL loading (wt.%) shows the ratio between the weight of IL inside the MOF and the weight of composite itself. 55.1% of [BMIM][BF_4]/MOF composites have IL loadings between 0.15 and 5 wt%, whereas 27.7% of them have IL loadings in the range of 5–10 wt%. Higher loadings are less common; 12.4, 3.7, and 0.8% of [BMIM][BF_4]/MOF composites have IL loadings of 10–15, 15–20, and 20–30 wt%, respectively. Fig. 5(b) shows the percentage of composites that were computed to be three-times more CO_2 selective than their corresponding MOFs for different ranges of IL loading. For example, 3 of 8 (17 of 40) composites that have IL loadings of 20–30 (15–20) wt.% were three-times more CO_2 selective compared to their corresponding pristine MOFs. Our results clearly showed that increasing the IL loading enhances the CO_2/N_2 selectivity of IL/MOF composites, consistent with the previous experimental reports [21,51].

We finally focused on the structure-performance relations and investigated the effect of pore size on the selectivity of [BMIM][BF_4]/MOF composites. MOFs with narrow pore sizes, specifically PLDs between 3.8 and 5 Å were predicted to have the highest performance for CO_2 separation from CO_2/N_2 mixture in the literature [53]. Fig. 6(a) demonstrates CO_2/N_2 selectivities of pristine MOFs and [BMIM][BF_4]/MOF composites as a function of their PLDs. The likelihood of having a higher selectivity increases with decreasing PLD for both pristine MOFs and [BMIM][BF_4]/MOF composites. Here it is important to note that composites with PLDs < 3.3 Å were computed to have LCDs > 4.1 Å indicating that gas molecules would still be able to adsorb in these pores. We also note that CO_2 molecules can be also located in the space between the ions of the IL and/or around the side chain of the imidazolium ring of the IL inside the MOF pore [68,69]. Normalized CO_2/N_2 selectivities of the composites were plotted as a function of the reduction of materials' PLDs upon IL incorporation in Fig. 6(b). Four of eight [BMIM][BF_4]/MOF composites that are at least ten-times more selective than their corresponding pristine MOFs showed a decrease in their PLDs in the range of 50–70% while PLDs of the other half were decreased by 70–90%. All these results suggest that the high affinity of IL towards CO_2 and reduction in the PLD upon IL incorporation are the main reasons of increased CO_2/N_2 selectivities of [BMIM][BF_4]/MOF

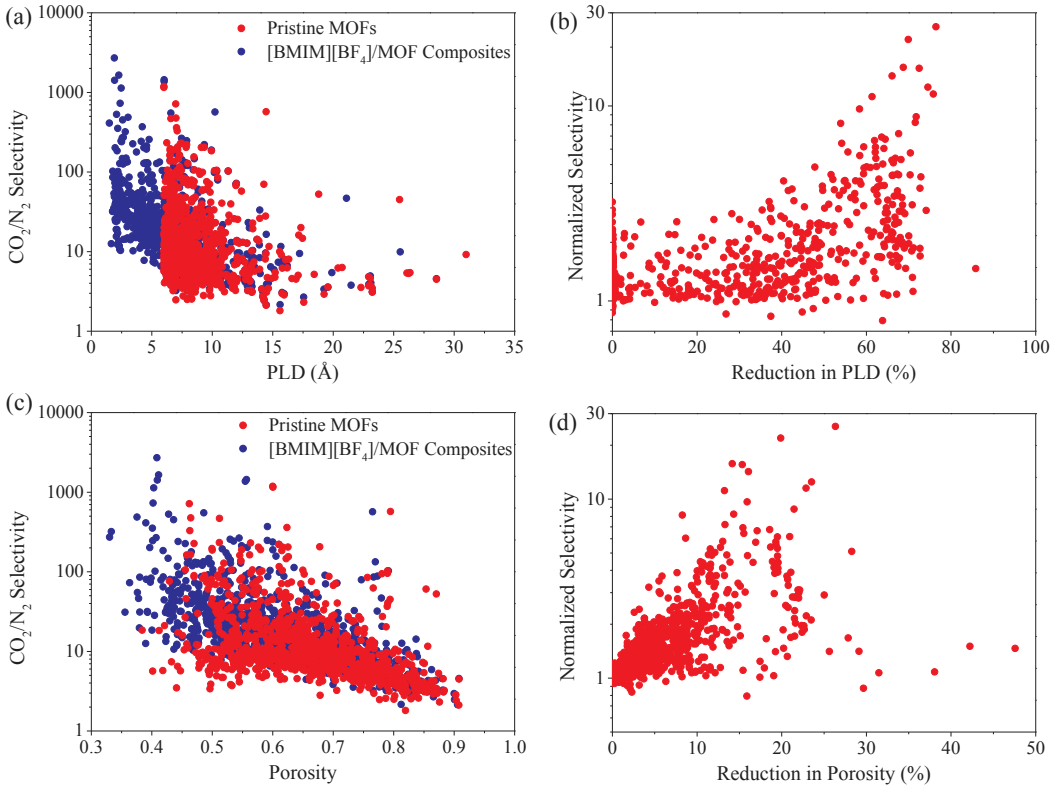


Fig. 6. (a, c) CO_2/N_2 selectivities of [BMIM][BF_4]/MOF composites and pristine MOFs as a function of their PLDs and porosities. (b, d) Normalized selectivities of [BMIM][BF_4]/MOF composites as a function of reduction in their PLDs and porosities upon the IL incorporation.

composites.

Fig. 6(c) shows CO_2 selectivities of [BMIM][BF_4]/MOF composites and pristine MOFs as a function of their porosities and changes in the porosity and selectivity upon [BMIM][BF_4] incorporation. Results showed that MOFs and [BMIM][BF_4]/MOF composites with higher CO_2/N_2 selectivities have lower porosities than others. Fig. 6(d) represents the normalized selectivities of composites as a function of the reduction in their porosities. The decrease in porosity upon IL incorporation leads to an enhancement in selectivity and the likelihood of having an enhanced selectivity increases with the higher reduction in the porosity similar to the effect of reduced PLD. When we consider 11 composites that showed 25–50% lower porosity than their pristine MOFs, two of them are at least three-times more selective than their corresponding MOFs. Only 12 composites were at least three-times more selective than their pristine MOFs when we consider 880 composites that showed 0–10% lower porosity upon IL incorporation, even though most of them offer enhanced selectivity. Our results suggest that the decrease in porosities upon IL incorporation is another reason behind the enhanced CO_2/N_2 separation performance of IL/MOF composites.

In order to better understand the increase in CO_2/N_2 selectivity of MOFs upon the incorporation of [BMIM][BF_4], we compared the Q_{st} values obtained from GCMC simulations for the adsorption of CO_2/N_2 mixture in pristine MOFs with those obtained for [BMIM][BF_4]-incorporated MOFs in Fig. 7(a). Higher Q_{st} values of composites than those of MOFs support the stronger interaction between the guest molecules and IL/MOF composites. We also examined the relation between the change in the Q_{st} values ($\Delta Q_{st} = Q_{st,Composite}-Q_{st,MOF}$) as a function of the reduction in the porosity upon incorporation of [BMIM][BF_4] into the frameworks in Fig. 7(b). The difference in the calculated Q_{st} values of composites and MOFs increases as the reduction in porosity due to IL incorporation increases. This result suggests that reduction in the porosity, hence stronger confinement of the guest molecules in the materials' pores, is one of the reasons behind the enhanced Q_{st} values of composites. The relation between normalized CO_2/N_2 selectivities and the change in Q_{st} upon IL incorporation is shown in Fig. 7(c). Normalized selectivity increases exponentially as the change in Q_{st} increases and these two were found to be highly correlated with a correlation coefficient of 0.95. Fig. 7(c) suggests that once the $\Delta Q_{st} > 15$ kJ/mol, an IL-incorporated MOF is expected to have at least ten-times higher CO_2/N_2 selectivity than its pristine counterpart. Overall, the change in chemical environment of the framework and reduction in the porosity are mainly responsible for the enhanced CO_2/N_2 selectivity of IL/MOF composites.

4. Conclusions

In this work, we used a high-throughput computational screening approach to uncover CO_2/N_2 mixture separation potentials of 1085 different [BMIM][BF_4]/MOF composites. The accuracy of our molecular simulation methodology was demonstrated by comparing experimental and simulated CO_2/N_2 selectivities and CO_2 working capacities of three different [BMIM][BF_4]/MOF composites, which were synthesized and characterized in detail. Results of high-throughput molecular simulations showed that [BMIM][BF_4] incorporation can significantly increase CO_2 selectivity (up to 25-times), CO_2 working capacity (up to six-times) and APS (up to 81-times) of pristine MOFs. Increasing the IL loading leads to decreased PLDs and porosities which improved CO_2/N_2 selectivities of [BMIM][BF_4]/MOF composites. Overall, we showed the great potential of IL/MOF composites composed of a single type of IL and > 1000 types of MOFs for separation of flue gas mixtures. Considering the availability of theoretically infinite number of IL-MOF combinations, our results will be highly useful for the design and development of new and novel IL/MOF composites with an extraordinarily high CO_2 separation performance.

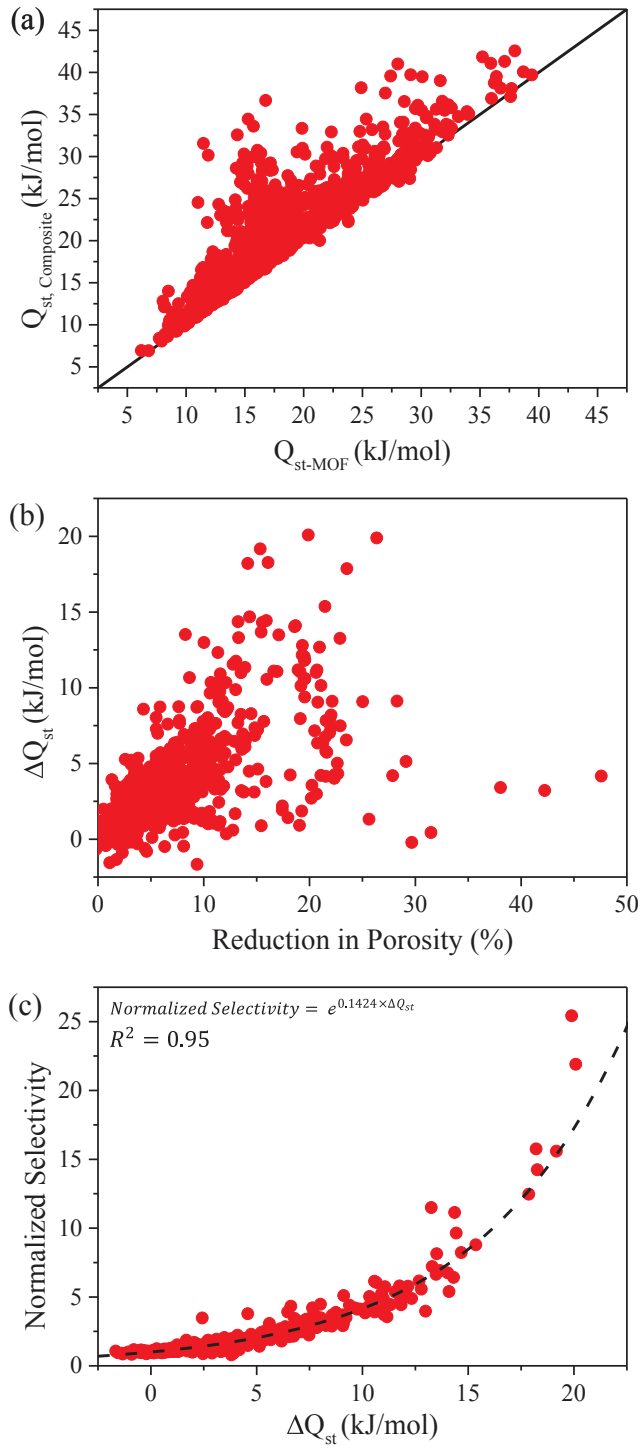


Fig. 7. (a) Comparison of Q_{st} values of composites and pristine MOFs. (b) Change in the Q_{st} values as a function of the reduction in porosity upon incorporation of [BMIM][BF_4]. (c) Normalized CO_2/N_2 selectivities as a function of the change in Q_{st} values upon incorporation of [BMIM][BF_4]. Dashed line in (c) shows the exponential function given in the inset.

Acknowledgements

S.K. acknowledges ERC-2017-Starting Grant. This research has received funding from the European Research Council (ERC) under the European Union's Horizon 2020 research and innovation programme (ERC-2017-Starting Grant, grant agreement No 756489-COSMOS). Authors thank Çiğdem Altıntaş and Hilal Dağlar for their support in simulation of MOF structures. We acknowledge Koç University Seed Fund Program, the Scientific and Technological Research Council of Turkey (TUBITAK) under 1001-Scientific and Technological Research Projects Funding Program (project number: 114R093), Koç University TÜPRAŞ Energy Center (KUTEM), Koç University Surface Science and Technology Center (KUYTAM), and TARLA for the collaborative research support.

Appendix A. Supplementary data

Supplementary data to this article can be found online at https://doi.org/10.1016/j.cej.2020.124916.

References

[1] A. Sayari, Y. Belmabkhout, R. Serna-Guerrero, Flue gas treatment via CO_2 adsorption, Chem. Eng. J. 171 (2011) 760–774.
[2] M.R. Raupach, G. Marland, P. Ciais, C. Le Quere, J.G. Canadell, G. Klepper, C.B. Field, Global and regional drivers of accelerating CO_2 emissions, Proc. Natl. Acad. Sci. 104 (2007) 10288–10293.
[3] P. Luis, Use of monoethanolamine (MEA) for CO_2 capture in a global scenario: Consequences and alternatives, Desalination. 380 (2016) 93–99.
[4] Y. Tokuda, E. Fujisawa, N. Okabayashi, N. Matsumiya, K. Takagi, H. Mano, K. Haraya, M. Sato, Development of hollow fiber membranes for CO_2 separation, Energy Convers. Manag. 38 (1997) S111–S116.
[5] C.F. Song, Y. Kitamura, S.H. Li, W.Z. Jiang, Parametric Analysis of a Novel Cryogenic CO_2 Capture System Based on Stirling Coolers, Environ. Sci. Technol. 46 (2012) 12735–12741.
[6] Z. Yuan, M.R. Eden, R. Gani, Toward the Development and Deployment of Large-Scale Carbon Dioxide Capture and Conversion Processes, Ind. Eng. Chem. Res. 55 (2016) 3383–3419.
[7] L. Estevez, D. Barpaga, J. Zheng, S. Sabale, R.L. Patel, J.-G. Zhang, B.P. McGrail, R.K. Motkuri, Hierarchically Porous Carbon Materials for CO_2 Capture: The Role of Pore Structure, Ind. Eng. Chem. Res. 57 (2018) 1262–1268.
[8] Y. Jiang, J. Ling, P. Xiao, Y. He, Q. Zhao, Z. Chu, Y. Liu, Z. Li, P.A. Webley, Simultaneous biogas purification and CO_2 capture by vacuum swing adsorption using zeolite NaUSY, Chem. Eng. J. 334 (2018) 2593–2602.
[9] S. Keskin, D.S. Sholl, Selecting metal organic frameworks as enabling materials in mixed matrix membranes for high efficiency natural gas purification, Energy Environ. Sci. 3 (2010) 343–351.
[10] J. Yu, L.-H. Xie, J.-R. Li, Y. Ma, J.M. Seminario, P.B. Balbuena, CO_2 Capture and Separations Using MOFs: Computational and Experimental Studies, Chem. Rev. 117 (2017) 9674–9754.
[11] H. Furukawa, K.E. Cordova, M. O'Keeffe, O.M. Yaghi, The chemistry and applications of metal-organic frameworks, Science 80- (2013) 341.
[12] S. Keskin, Screening for selectivity, Nat. Energy. (2019).
[13] A. Uzun, S. Keskin, Site characteristics in metal organic frameworks for gas adsorption, Prog. Surf. Sci. 89 (2014) 56–79.
[14] Y. Zhang, J. Zhou, X. Chen, L. Wang, W. Cai, Coupling of heterogeneous advanced oxidation processes and photocatalysis in efficient degradation of tetracycline hydrochloride by Fe-based MOFs: Synergistic effect and degradation pathway, Chem. Eng. J. 369 (2019) 745–757.
[15] R. Zhao, Z. Liang, R. Zou, Q. Xu, Metal-Organic Frameworks for Batteries, Joule. 2 (2018) 2235–2259.
[16] S.-W. Lv, J.-M. Liu, C.-Y. Li, N. Zhao, Z.-H. Wang, S. Wang, A novel and universal metal-organic frameworks sensing platform for selective detection and efficient removal of heavy metal ions, Chem. Eng. J. 375 (2019) 122111.
[17] J. Pang, F. Jiang, M. Wu, C. Liu, K. Su, W. Lu, D. Yuan, M. Hong, A porous metal-organic framework with ultrahigh acetylene uptake capacity under ambient conditions, Nat. Commun. 6 (2015) 1–7.
[18] X.-J. Wang, P.-Z. Li, Y. Chen, Q. Zhang, H. Zhang, X.X. Chan, R. Ganguly, Y. Li, J. Jiang, Y. Zhao, A Rationally Designed Nitrogen-Rich Metal-Organic Framework and Its Exceptionally High CO_2 and H_2 Uptake Capability, Sci. Rep. 3 (2013) 1149.
[19] J. Jiang, H. Furukawa, Y.B. Zhang, O.M. Yaghi, High Methane Storage Working Capacity in Metal-Organic Frameworks with Acrylate Links, J. Am. Chem. Soc. 138 (2016) 10244–10251.
[20] B. Wang, H. Huang, X.-L. Lv, Y. Xie, M. Li, J.-R. Li, Tuning CO_2 Selective Adsorption over N_2 and CH_4 in UiO-67 Analogues through Ligand Functionalization, Inorg. Chem. 53 (2014) 9254–9259.
[21] K.B. Sezginel, S. Keskin, A. Uzun, Tuning the Gas Separation Performance of CuBTC by Ionic Liquid Incorporation, Langmuir. 32 (2016) 1139–1147.
[22] M. Mohamedali, H. Ibrahim, A. Henni, Incorporation of acetate-based ionic liquids into a zeolitic imidazolate framework (ZIF-8) as e ffi cient sorbents for carbon dioxide capture, Chem. Eng. J. 334 (2018) 817–828.
[23] F.P. Kinik, A. Uzun, S. Keskin, Ionic Liquid/Metal–Organic Framework Composites: From Synthesis to Applications, ChemSusChem. 10 (2017) 2842–2863.
[24] Z. Lei, B. Chen, Y.M. Koo, D.R. Macfarlane, Introduction: Ionic Liquids, Chem. Rev. 117 (2017) 6633–6635.
[25] C. Verma, E.E. Ebenso, M.A. Quraishi, Transition metal nanoparticles in ionic liquids: Synthesis and stabilization, J. Mol. Liq. 276 (2019) 826–849.
[26] J. Zhao, Y. Yue, G. Sheng, B. Wang, H. Lai, S. Di, Y. Zhai, L. Guo, X. Li, Supported

ionic liquid-palladium catalyst for the highly effective hydrochlorination of acetylene, Chem. Eng. J. 360 (2019) 38–46.
[27] P. Sharma, S. Do Park, K.T. Park, S.C. Nam, S.K. Jeong, Y. Il Yoon, I.H. Baek, Solubility of carbon dioxide in amine-functionalized ionic liquids: Role of the anions, Chem. Eng. J. 193–194 (2012) 267–275.
[28] M. Ramdin, T.W. de Loos, T.J.H. Vlugt, State-of-the-Art of CO_2 Capture with Ionic Liquids, Ind. Eng. Chem. Res. 51 (2012) 8149–8177.
[29] M. Zeeshan, V. Nozari, M.B. Yagci, T. Islk, U. Unal, V. Ortalan, S. Keskin, A. Uzun, Core-Shell Type Ionic Liquid/Metal Organic Framework Composite: An Exceptionally High CO_2/CH_4 Selectivity, J. Am. Chem. Soc. 140 (2018) 10113–10116.
[30] F.P. Kinik, C. Altintas, V. Balci, B. Koyuturk, A. Uzun, S. Keskin, [BMIM][PF_6] Incorporation Doubles CO_2 Selectivity of ZIF-8: Elucidation of Interactions and Their Consequences on Performance, ACS Appl. Mater. Interfaces. 8 (2016) 30992–31005.
[31] H. Kulak, H.M. Polat, S. Kavak, S. Keskin, A. Uzun, Improving CO_2 Separation Performance of MIL-53(Al) by Incorporating 1-n-Butyl-3-Methylimidazolium Methyl Sulfate, Energy Technol. 7 (2019) 1900157.
[32] S. Kavak, H.M. Polat, H. Kulak, S. Keskin, A. Uzun, MIL-53(Al) as a Versatile Platform for Ionic-Liquid/MOF Composites to Enhance CO_2 Selectivity over CH_4 and N_2, Chem. – An Asian J. 14 (2019) 3655–3667.
[33] T. Düren, Y.-S. Bae, R.Q. Snurr, Using molecular simulation to characterise metal–organic frameworks for adsorption applications, Chem. Soc. Rev. 38 (2009) 1237–1247.
[34] I. Erucar, S. Keskin, High-Throughput Molecular Simulations of Metal Organic Frameworks for CO_2 Separation: Opportunities and Challenges, Front. Mater. 5 (2018) 4.
[35] A. Sturluson, M.T. Huynh, A.R. Kaija, C. Laird, S. Yoon, F. Hou, Z. Feng, C.E. Wilmer, Y.J. Colón, Y.G. Chung, D.W. Siderius, C.M. Simon, The role of molecular modelling and simulation in the discovery and deployment of metal-organic frameworks for gas storage and separation, Mol. Simul. 45 (2019) 1082–1121.
[36] H. Xing, X. Zhao, Q. Yang, B. Su, Z. Bao, Y. Yang, Q. Ren, Molecular dynamics simulation study on the absorption of ethylene and acetylene in ionic liquids, Ind. Eng. Chem. Res. 52 (2013) 9308–9316.
[37] E. Núñez-Rojas, H.M. Flores-Ruiz, J. Alejandre, Molecular dynamics simulations to separate benzene from hydrocarbons using polar and ionic liquid solvents, J. Mol. Liq. 249 (2018) 591–599.
[38] X. Liu, G. Zhou, X. Zhang, S. Zhang, Molecular dynamics simulation of desulfurization by ionic liquids, AIChE J. 56 (2010) 2983–2996.
[39] H. Cheng, J. Zhang, Z. Qi, Effects of interaction with sulphur compounds and free volume in imidazolium-based ionic liquid on desulphurisation: a molecular dynamics study, Mol. Simul. 44 (2018) 55–62.
[40] L.X. Dang, T.-M. Chang, Molecular Mechanism of Gas Adsorption into Ionic Liquids: A Molecular Dynamics Study, J. Phys. Chem. Lett. 3 (2012) 175–181.
[41] Y. Chen, Z. Hu, K.M. Gupta, J. Jiang, Ionic liquid/metal-organic framework composite for CO_2 capture: A computational investigation, J. Phys. Chem. C. 115 (2011) 21736–21742.
[42] J.M. Vicent-Luna, J.J. Gutiérrez-Sevillano, J.A. Anta, S. Calero, Effect of room-temperature ionic liquids on CO_2 separation by a Cu-BTC metal-organic framework, J. Phys. Chem. C. 117 (2013) 20762–20768.
[43] W. Xue, Z. Li, H. Huang, Q. Yang, D. Liu, Q. Xu, C. Zhong, Effects of ionic liquid dispersion in metal-organic frameworks and covalent organic frameworks on CO_2 capture: A computational study, Chem. Eng. Sci. 140 (2016) 1–9.
[44] J.M. Vicent-Luna, J.J. Gutiérrez-Sevillano, S. Hamad, J. Anta, S. Calero, Role of Ionic Liquid $[EMIM]^+[SCN]^-$ in the Adsorption and Diffusion of Gases in Metal-Organic Frameworks, ACS Appl. Mater. Interfaces. 10 (2018) 29694–29704.
[45] K.M. Gupta, Y. Chen, Z. Hu, J. Jiang, Metal-organic framework supported ionic liquid membranes for CO_2 capture: Anion effects, Phys. Chem. Chem. Phys. 14 (2012) 5785–5794.
[46] K.M. Gupta, Y. Chen, J. Jiang, Ionic liquid membranes supported by hydrophobic and hydrophilic metal-organic frameworks for CO_2 capture, J. Phys. Chem. C. 117 (2013) 5792–5799.
[47] Y. Lan, T. Yan, M. Tong, C. Zhong, Large-scale computational assembly of ionic liquid/MOF composites: Synergistic effect in the wire-tube conformation for efficient CO_2/CH_4 separation, J. Mater. Chem. A. 7 (2019) 12556–12564.
[48] Z. Li, Y. Xiao, W. Xue, Q. Yang, C. Zhong, Ionic liquid/metal-organic framework composites for H_2S removal from natural gas: A computational exploration, J. Phys. Chem. C. 119 (2015) 3674–3683.
[49] J.M. Vicent-Luna, A. Luna-Triguero, S. Calero, Storage and Separation of Carbon Dioxide and Methane in Hydrated Covalent Organic Frameworks, J. Phys. Chem. C. 120 (2016) 23756–23762.
[50] A. Ahmed, A.J. Matzger, S. Seth, J. Purewal, A.G. Wong-foy, M. Veenstra, D.J. Siegel, Exceptional hydrogen storage achieved by screening nearly half a million metal-organic frameworks, Nat. Commun. 10 (2019) 1568.
[51] B. Koyuturk, C. Altintas, F.P. Kinik, S. Keskin, A. Uzun, Improving Gas Separation Performance of ZIF-8 by [BMIM][BF_4] Incorporation: Interactions and Their Consequences on Performance, J. Phys. Chem. C. 121 (2017) 10370–10381.
[52] H.M. Polat, M. Zeeshan, A. Uzun, S. Keskin, Unlocking CO_2 separation performance of ionic liquid/CuBTC composites: Combining experiments with molecular simulations, Chem. Eng. J. 373 (2019).
[53] C. Altintas, G. Avci, H. Daglar, A. Nemati Vesali Azar, S. Velioglu, I. Erucar, S. Keskin, Database for CO_2 Separation Performances of MOFs Based on Computational Materials Screening, ACS Appl. Mater. Interfaces. 10 (2018) 17257–17268.
[54] P.Z. Moghadam, A. Li, S.B. Wiggin, A. Tao, A.G.P. Maloney, P.A. Wood, S.C. Ward, D. Fairen-Jimenez, Development of a Cambridge Structural Database Subset: A Collection of Metal-Organic Frameworks for Past, Present, and Future, Chem. Mater. 29 (2017) 2618–2625.
[55] D. Dubbeldam, S. Calero, D.E. Ellis, R.Q. Snurr, RASPA: Molecular simulation software for adsorption and diffusion in flexible nanoporous materials, Mol. Simul. 42 (2016) 81–101.
[56] S.L. Mayo, B.D. Olafson, W.A. Goddard, DREIDING: A generic force field for molecular simulations, J. Phys. Chem. 94 (1990) 8897–8909.
[57] A.K. Rappe, C.J. Casewit, K.S. Colwell, W.A. Goddard, W.M. Skiff, UFF, a full periodic table force field for molecular mechanics and molecular dynamics simulations, J. Am. Chem. Soc. 114 (1992) 10024–10035.
[58] J.J. Potoff, J.I. Siepmann, Vapor–liquid equilibria of mixtures containing alkanes, carbon dioxide, and nitrogen, AIChE J. 47 (2001) 1676–1682.
[59] K. Makrodimitris, G.K. Papadopoulos, D.N. Theodorou, Prediction of permeation properties of CO_2 and N_2 through silicalite via molecular simulations, J. Phys. Chem. B. 105 (2001) 777–788.
[60] L. Zhao, Q. Yang, Q. Ma, C. Zhong, J. Mi, D. Liu, A force field for dynamic Cu-BTC metal-organic framework, J. Mol. Model. 17 (2011) 227–234.
[61] T.F. Willems, C.H. Rycroft, M. Kazi, J.C. Meza, M. Haranczyk, Algorithms and tools for high-throughput geometry-based analysis of crystalline porous materials, Microporous Mesoporous Mater. 149 (2012) 134–141.
[62] C.E. Wilmer, R.Q. Snurr, Towards rapid computational screening of metal-organic frameworks for carbon dioxide capture: Calculation of framework charges via charge equilibration, Chem. Eng. J. 171 (2011) 775–781.
[63] Y.-S. Bae, R.Q. Snurr, Development and Evaluation of Porous Materials for Carbon Dioxide Separation and Capture, Angew. Chemie Int. Ed. 50 (2011) 11586–11596.
[64] Accelrys, Materials Studio 18.1, (2018).
[65] M. Babucci, C.Y. Fang, J.E. Perez-Aguilar, A.S. Hoffman, A. Boubnov, E. Guan, S.R. Bare, B.C. Gates, A. Uzun, Controlling catalytic activity and selectivity for partial hydrogenation by tuning the environment around active sites in iridium complexes bonded to supports, Chem. Sci. 10 (2019) 2623–2632.
[66] N.E. Heimer, R.E. Del Sesto, Z. Meng, J.S. Wilkes, W.R. Carper, Vibrational spectra of imidazolium tetrafluoroborate ionic liquids, J. Mol. Liq. 124 (2006) 84–95.
[67] S. Cha, M. Ao, W. Sung, B. Moon, B. Ahlström, P. Johansson, Y. Ouchi, D. Kim, Structures of ionic liquid–water mixtures investigated by IR and NMR spectroscopy, Phys. Chem. Chem. Phys. 16 (2014) 9591–9601.
[68] O. Hollóczki, Z. Kelemen, L. Kçnczçl, D. Szieberth, Significant Cation Effects in Carbon Dioxide – Ionic Liquid Systems, ChemPhysChem. 14 (2013) 315–320.
[69] M. Kanakubo, T. Aizawa, H. Nanjo, Y. Kameda, Y. Amo, T. Usuki, Liquid structures of 1-butyl-3-methylimidazolium tetrafluoroborate and carbon dioxide mixtures by X-ray diffraction measurements, Fluid Phase Equilib. 297 (2010) 183–186.